

Probing the hyperbolic branch/focus point region of the constrained minimal supersymmetric standard model with generalized Yukawa quasi-unification

N. Karagiannakis,^{1,*} G. Lazarides,^{1,†} and C. Pallis^{2,‡}

¹*School of Electrical and Computer Engineering, Faculty of Engineering,
Aristotle University of Thessaloniki, Thessaloniki 54124, Greece*

²*Departament de Física Teòrica and IFIC, Departament de Física Teòrica and IFIC, E-46100 Burjassot, SPAIN*
(Dated: March 4, 2022)

We analyze the parametric space of the constrained minimal supersymmetric standard model with $\mu > 0$ supplemented by a generalized asymptotic Yukawa coupling quasi-unification condition which yields acceptable masses for the fermions of the third family. We impose constraints from the cold dark matter abundance in the universe and its direct detection experiments, the B -physics, as well as the masses of the sparticles and the lightest neutral CP-even Higgs boson. Fixing the mass of the latter to its central value from the LHC and taking $40 \lesssim \tan \beta \lesssim 50$, we find a relatively wide allowed parameter space with $-11 \lesssim A_0/M_{1/2} \lesssim 15$ and mass of the lightest sparticle in the range $(0.09 - 1.1)$ TeV. This sparticle is possibly detectable by the present cold dark matter direct search experiments. The required fine-tuning for the electroweak symmetry breaking is much milder than the one needed in the neutralino-stau coannihilation region of the same model.

PACS numbers: 12.10.Kt, 12.60.Jv, 95.35.+d, 14.80.Cp; **Published in** Phys. Rev. D **92**, no. 8, 085018 (2015)

I. INTRODUCTION

The well-known *constrained minimal supersymmetric standard model* (CMSSM) [1–8] is a highly predictive version of the *minimal supersymmetric standard model* (MSSM). Its basic characteristic is that it employs universal boundary conditions for the soft *supersymmetry* (SUSY) breaking terms. Namely, the free parameters of the CMSSM are the following

$$\text{sign}\mu, \tan\beta, M_{1/2}, m_0, \text{ and } A_0, \quad (1)$$

where $\text{sign}\mu$ is the sign of μ , the mass parameter mixing the electroweak Higgs superfields H_2 and H_1 of the MSSM which couple to the up- and down-type quarks respectively, $\tan\beta$ is the ratio of the vacuum expectation values of H_2 and H_1 , while the remaining symbols denote the common gaugino mass, the common scalar mass, and the common trilinear scalar coupling constant, respectively, defined at the *grand unified theory* (GUT) scale M_{GUT} , which is determined by the unification of the gauge coupling constants.

However, the recently announced experimental data on the mass of the *standard model* (SM)-like Higgs boson [9, 10] and the branching ratio $\text{BR}(B_s \rightarrow \mu^+\mu^-)$ of the process $B_s \rightarrow \mu^+\mu^-$ [11–13] in conjunction with the upper bound [14] from *cold dark matter* (CDM) considerations on the relic abundance $\Omega_{\text{LSP}}h^2$ of the *lightest SUSY particle* (LSP) – which is the lightest neutralino $\tilde{\chi}$ – put under considerable stress [15–18] the parameter space of the CMSSM. It is by now clear, however, that there still exist viable slices of the following three regions

of the parameter space of the CMSSM which give acceptable values of $\Omega_{\text{LSP}}h^2$:

- (i) *The neutralino-stau* ($\tilde{\chi} - \tilde{\tau}_1$) *coannihilation region* with $M_{1/2} \gg m_0$, where $\tilde{\chi}$ is an almost pure bino and $\Omega_{\text{LSP}}h^2$ is reduced to an acceptable level due to the proximity between the mass m_{LSP} of the LSP and the mass $m_{\tilde{\tau}_1}$ of the lightest stau $\tilde{\tau}_1$, which is the *next-to-LSP* (NLSP).
- (ii) *The A-funnel region* [15] appearing at large ($\gtrsim 40$) $\tan\beta$ values, where the mass m_A of the CP-odd Higgs boson A satisfies the relation $m_A \simeq 2m_{\text{LSP}}$ and so the $\tilde{\chi} - \tilde{\chi}$ pair annihilation procedure is enhanced by an A -pole exchange in the s -channel, thereby reducing $\Omega_{\text{LSP}}h^2$.
- (iii) *The hyperbolic branch/focus point (HB/FP) region* [19–27] located at large values of $m_0 \gg M_{1/2}$ and small μ 's, which ensures a sizable higgsino fraction of $\tilde{\chi}$. The $\Omega_{\text{LSP}}h^2$ remains under control for $m_{\text{LSP}} \lesssim 1$ TeV thanks to the rapid $\tilde{\chi} - \tilde{\chi}$ annihilation and the neutralino-chargino ($\tilde{\chi}/\tilde{\chi}_2 - \tilde{\chi}_1^+$) coannihilation [28–30] ($\tilde{\chi}_2$ is the next-to-lightest neutralino and $\tilde{\chi}_1^+$ the lightest chargino).

It would be interesting to investigate whether this available parameter space survives in even more restrictive versions of the CMSSM, which can emerge by embedding it in concrete SUSY GUT models. Here we focus on the *Pati-Salam* (PS) GUT model based on the gauge group $G_{\text{PS}} = SU(4)_c \times SU(2)_L \times SU(2)_R$ [31, 32]. It is interesting to note that this model can arise [33, 34] from the standard weakly coupled heterotic string and the D-brane setups [35, 36] and its phenomenology has been extensively studied – see e.g. Ref. [37]. It can also naturally arise in the framework of non-commutative geometry [38].

*Electronic address: nikar@auth.gr

†Electronic address: lazaride@eng.auth.gr

‡Electronic address: cpallis@ific.uv.es

The SUSY PS model in its simplest realization leads [39] to ‘asymptotic’ *Yukawa unification* (YU) [40, 41], i.e. the exact unification, at the GUT scale M_{GUT} , of the Yukawa coupling constants h_t , h_b , and h_τ of the top quark t , the bottom quark b , and the tau lepton τ , respectively. Although the CMSSM with YU is an elegant model, it yields unacceptable values of the b -quark mass m_b for both signs of μ given the experimental values of the t and τ masses – which, combined with YU, naturally restrict $\tan\beta$ to large values. This is due to the presence of sizable SUSY corrections [42–45] to the tree-level b -quark mass (about 20%), which drive it well above [a little below] its 95% *confidence level* (c.l.) experimental range for $\mu > 0$ [$\mu < 0$] – we use the standard convention of Ref. [46] for the sign of μ .

In order to circumvent this difficulty, we consider here the extended PS SUSY GUT model introduced in Ref. [47] and reviewed in Refs. [48, 49], which yields a moderate deviation from exact YU and, thus, allows acceptable values of the b -quark mass for both signs of μ within the CMSSM. In particular, the Higgs sector of the simplest PS model [31, 32] is extended so that H_2 and H_1 are not exclusively contained in a $SU(4)_c$ singlet, $SU(2)_L \times SU(2)_R$ bidoublet superfield, but receive subdominant contributions from another bidoublet too which belongs to the adjoint representation of $SU(4)_c$. As a result, YU is naturally violated and replaced by a set of asymptotic Yukawa quasi-unification (YQU) conditions:

$$h_t(M_{\text{GUT}}) : h_b(M_{\text{GUT}}) : h_\tau(M_{\text{GUT}}) = \left| \frac{1 - \rho\alpha_2/\sqrt{3}}{\sqrt{1 + |\alpha_2|^2}} \right| : \left| \frac{1 - \rho\alpha_1/\sqrt{3}}{\sqrt{1 + |\alpha_1|^2}} \right| : \left| \frac{1 + \sqrt{3}\rho\alpha_1}{\sqrt{1 + |\alpha_1|^2}} \right|. \quad (2)$$

These conditions depend on two complex parameters α_1 , α_2 and one real and positive parameter ρ . The parameters α_1 and α_2 describe the mixing of the components of the $SU(4)_c$ singlet and 15-plet Higgs bidoublets, while ρ is the ratio of their respective Yukawa coupling constants to the fermions of the third family [49, 50].

In our original papers [47, 51–54], we have considered monoparametric versions of the YQU conditions depending on just one parameter, which was considered for simplicity real and replaced $\tan\beta$ in the investigation of the parametric space of the model. These forms of the YQU conditions arise by taking $\alpha_1 = -\alpha_2$ for $\mu > 0$ or $\alpha_1 = \alpha_2$ for $\mu < 0$. Indeed, these choices turn out to be suitable for generating an adequate violation of YU and ensuring, at the same time, successful radiative *electroweak symmetry breaking* (EWSB) and the presence of a neutralino LSP in a large fraction of the parametric space. However, the emergent versions of CMSSM are by now experimentally excluded. For $\mu < 0$, this is due to the incompatibility between the bound on the branching ratio $\text{BR}(b \rightarrow s\gamma)$ of the process $b \rightarrow s\gamma$ and the CDM constraints [51]. For $\mu > 0$, on the other hand, it is due to the fact that the parameter space where the CDM constraint on $\Omega_{\text{LSP}}h^2$ is satisfied thanks to $\tilde{\chi} - \tilde{\tau}_1$ coannihilations

turns out to be non-overlapping with the space allowed by the data [11, 12] on $\text{BR}(B_s \rightarrow \mu^+\mu^-)$ [54]. The main reason for the latter negative result is that $\tan\beta$ remains large and, hence, it enhances the SUSY contribution to $\text{BR}(B_s \rightarrow \mu^+\mu^-)$.

In order to overcome this hurdle, we adopted in Refs. [49, 50] the more general version of Eq. (2) without imposing any relation between α_1 and α_2 . As a consequence, we could accommodate more general values of the ratios h_m/h_n with $m, n = t, b, \tau$ – still of order unity for natural values of the model parameters – and lower $\tan\beta$'s. The allowed parameter space of the model found in Ref. [50] is then mainly determined by the interplay between the constraints from the $\text{BR}(B_s \rightarrow \mu^+\mu^-)$, CDM, and the results of LHC on the Higgs boson h mass m_h . Actually, our acceptable solutions are due to a synergy between $\tilde{\chi} - \tilde{\tau}_1$ coannihilation and the A -funnel mechanism – see points (i) and (ii) above – given that $m_H \simeq m_A$ (H is the heavier CP-even neutral Higgs boson with mass m_H). However, m_{LSP} comes out to be large (~ 1 TeV), which makes the direct detectability of the LSP very difficult and the sparticle spectrum very heavy. Furthermore, the emergent values of $M_{1/2}$, m_0 , and μ lie in the multi-TeV range, which puts under some stress the naturalness of the radiative EWSB.

Therefore, the tantalizing question, which we address here, is whether the conditions in Eq. (2) can become compatible with the solutions obtained in the HB/FP region of the CMSSM – see point (iii) above. We show that this is not only possible but also quite promising since, apart from allowing a much wider parametric space, it gives smaller values of μ and m_{LSP} , despite the fact that m_0 and $M_{1/2}$ are quite large and the sfermions, sleptons and heavier Higgs bosons are quite heavy. Moreover, the LSP can be probed by the CDM detection experiments, which play a crucial role in limiting the parameter space of the model. Finally, the deviation needed from exact YU can be naturally attributed to the YQU conditions in Eq. (2), while the fine-tuning required for the radiative EWSB turns out to be milder than the one needed in the $\tilde{\chi} - \tilde{\tau}_1$ coannihilation region for m_{LSP} 's yielding $\Omega_{\text{LSP}}h^2$'s close to the cosmological upper bound.

We first (Sec. II) review the phenomenological and cosmological requirements which we consider in our investigation. Next (Sec. III), we exhibit the salient features of the HB/FP region of the CMSSM and find, in Sec. IV, the resulting restrictions on the parameters of the CMSSM. We, finally, check, in Sec. V, the consistency with Eq. (2) and discuss the naturalness of the model in Sec. VI. We summarize our conclusions in Sec. VII.

II. PHENOMENOLOGICAL AND COSMOLOGICAL CONSTRAINTS

In our investigation, we closely follow the renormalization group and radiative EWSB analysis of Refs. [49, 50]. Most notably, we use an optimal, common supersymmetric-

ric threshold

$$M_{\text{SUSY}} \simeq (m_{\tilde{t}_1} m_{\tilde{t}_2})^{1/2} \quad (3)$$

(with $\tilde{t}_{1,2}$ being the stop quark mass eigenstates) which reduces drastically the one-loop corrections to the Higgs boson masses, making their calculation from the tree-level effective potential quite accurate and stable [7]. The SUSY spectrum is also evaluated at M_{SUSY} by using the publicly available calculator `SOFTSUSY` [55]. The output is put into `micrOMEGAS` [56], a publicly available code, which calculates a number of phenomenological – see Sec. II A – and cosmological – see Sec. II B – observables assisting us to restrict the parametric space of our model.

A. Phenomenological Constraints

The phenomenological considerations which we take into account in our study are the following:

1. SM fermion masses

In order to determine with good precision the running of the Yukawa coupling constants, we have to take into account the sizable SUSY corrections [42–44, 57, 58] to the tree-level b -quark and τ -lepton masses. We incorporate them in our code using the formulas of Ref. [57] in accordance with the recent reanalysis of Ref. [45]. The result is to be compared with the experimental value of $m_b(M_Z)$. This is derived by using as an input parameter the $\overline{\text{MS}}$ value, which, at $1 - \sigma$, is [59]

$$m_b(m_b)^{\overline{\text{MS}}} = 4.18 \pm 0.03 \text{ GeV}. \quad (4)$$

This range is evolved up to M_Z using the central value $a_s(M_Z) = 0.1185$ [59] of the strong fine-structure constant at M_Z and then converted to the $\overline{\text{DR}}$ scheme in accordance with the analysis of Ref. [60]. We obtain

$$2.8 \lesssim m_b(M_Z)/\text{GeV} \lesssim 2.86 \quad (5)$$

at 68% c.l. with the central value being $m_b(M_Z) = 2.83$ GeV. Less important but not negligible (almost 4%) are the SUSY corrections [57] to the τ -lepton mass, which have the effect [47, 51] of slightly reducing $\tan \beta$. We take as input the central value [60]

$$m_\tau(M_Z) = 1.748 \text{ GeV} \quad (6)$$

of the $\overline{\text{DR}}$ τ -lepton mass at M_Z . Finally, as regards the t -quark mass, we take the latest $1 - \sigma$ result [61] on its pole mass ($M_t = 173.34 \pm 0.76$ GeV) and construct the 68% c.l. range for its running mass $m_t(m_t)$:

$$164.1 \lesssim m_t(m_t)/\text{GeV} \lesssim 165.56 \quad (7)$$

with the central value being $m_t(m_t) = 164.83$ GeV.

2. The mass of the lightest Higgs boson

The experiments ATLAS and CMS in the LHC discovered simultaneously a boson that looks very much like the expected SM Higgs boson. Its measured mass turns out to be [9, 10]

$$m_h = \begin{cases} 125.36 \pm 0.37 \text{ (stat.)} \pm 0.18 \text{ (sys.) GeV (ATLAS),} \\ 125.03^{+0.26}_{-0.27} \text{ (stat.)}^{+0.13}_{-0.15} \text{ (sys.) GeV (CMS).} \end{cases} \quad (8)$$

While there is no combined analysis of the two experiments yet, we can estimate the allowed 95% c.l. range of this mass including a theoretical uncertainty of about ± 1.5 GeV. This gives

$$122 \lesssim m_h/\text{GeV} \lesssim 128.5. \quad (9)$$

In most of the plots in Sec. IV, we set

$$m_h = 125.5 \text{ GeV}, \quad (10)$$

which lies well inside the experimental range from both ATLAS and CMS in Eq. (8).

3. Sparticles searches

The mass limits which are relevant for our investigation are the following:

a. Mass of the chargino The combined results of experiments that took place at LEP [62] showed that, regardless of the model, the lower bound on the mass of the charginos is

$$m_{\tilde{\chi}^\pm} \gtrsim 103.5 \text{ GeV}. \quad (11)$$

b. Mass of the gluino The present model dependent 95% c.l. lower bound on the mass of the gluino is [63]

$$m_{\tilde{g}} \gtrsim 1.3 \text{ TeV}. \quad (12)$$

It is well-known that such a heavy gluino spoils the success of several models which consider the HB/FP region [64–71]. However, as we will show, this does not happen in our case.

4. B-physics constraints

We also consider the following constraints originating from B -meson physics:

- The branching ratio $\text{BR}(B_s \rightarrow \mu^+ \mu^-)$ of the process $B_s \rightarrow \mu^+ \mu^-$ [72, 73] is to be consistent with the 95% c.l. experimental upper bound [11, 12]

$$\text{BR}(B_s \rightarrow \mu^+ \mu^-) \lesssim 4.2 \times 10^{-9}. \quad (13)$$

Although the most recent experimental result is [13]

$$1.1 \lesssim \text{BR}(B_s \rightarrow \mu^+ \mu^-)/10^{-9} \lesssim 6.4, \quad (14)$$

we use the more stringent upper bound in Eq. (13), since it is a combined result and, thus, much more reliable.

- The branching ratio $\text{BR}(b \rightarrow s\gamma)$ of $b \rightarrow s\gamma$ [74–77] must lie in the 95% c.l. range [78–80]

$$2.79 \times 10^{-4} \lesssim \text{BR}(b \rightarrow s\gamma) \lesssim 4.07 \times 10^{-4}. \quad (15)$$

- The ratio $R(B_u \rightarrow \tau\nu)$ of the CMSSM to the SM branching ratio of the process $B_u \rightarrow \tau\nu$ [73, 81] should be confined in the 95% c.l. range [78]

$$0.52 \lesssim R(B_u \rightarrow \tau\nu) \lesssim 2.04. \quad (16)$$

5. Muon anomalous magnetic moment

There is a discrepancy δa_μ between the measured value of the muon anomalous magnetic moment a_μ from its SM prediction. The latter, though, is not yet completely stabilized mainly because of the ambiguities in the calculation of the hadronic vacuum-polarization contribution. According to the evaluation of this contribution in Ref. [82], there is still a discrepancy between the findings based on the e^+e^- -annihilation data and the ones based on the τ -decay data. However, in Ref. [83], it is claimed that this discrepancy can be alleviated. Taking into account the recent and more reliable calculation based on the e^+e^- data [84], the complete tenth-order QED contribution [85], and the experimental measurements [86] of a_μ , we end up with a $2.9 - \sigma$ discrepancy

$$\delta a_\mu = (24.9 \pm 8.7) \times 10^{-10}, \quad (17a)$$

resulting to the following 95% c.l. range:

$$7.5 \times 10^{-10} \lesssim \delta a_\mu \lesssim 42.3 \times 10^{-10}. \quad (17b)$$

This δa_μ can be attributed to SUSY contributions calculated by using the formulas of Ref. [87]. The resulting δa_μ has the sign of μ and its absolute value decreases as m_{LSP} increases. Therefore, Eq. (17b) hints that the sign of μ has to be positive. Moreover, a lower [upper] bound on m_{LSP} can be derived from the upper [lower] bound in Eq. (17b). As it turns out, only the upper bound on m_{LSP} is relevant here. Taking into account the aforementioned computational instabilities and the fact that a discrepancy at the level of about $3 - \sigma$ cannot firmly establish a real deviation from the SM value, we restrict ourselves to just mentioning at which level Eq. (17a) is satisfied in the parameter space allowed by all the other constraints – cf. Refs. [15–18].

B. Cosmological Constraints

Our cosmological considerations include information from the CDM abundance and direct detection experiments quoted below.

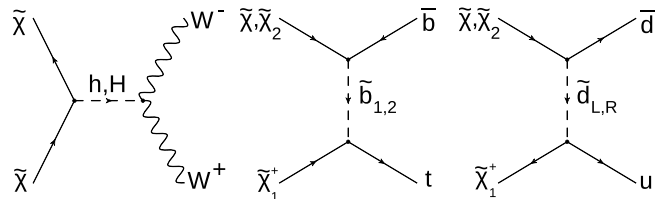


FIG. 1: Dominant $\tilde{\chi}-\tilde{\chi}$ annihilation and $\tilde{\chi}/\tilde{\chi}_2-\tilde{\chi}_1^+$ coannihilation reactions in the HB/FP region.

1. Cold dark matter abundance

In accordance with the recently reported results [14] from the Planck satellite, the 95% c.l. range for the CDM abundance in the universe is

$$\Omega_{\text{CDM}} h^2 = 0.1199 \pm 0.0054. \quad (18)$$

In the context of the CMSSM, the lightest neutralino $\tilde{\chi}$ can be the LSP and, thus, naturally arises as a CDM candidate as long as its relic abundance does not exceed the upper bound in Eq. (18), i.e.

$$\Omega_{\text{LSP}} h^2 \lesssim 0.125. \quad (19)$$

This is a quite strong restriction on the parameter space, since $\Omega_{\text{LSP}} h^2$ increases, in general, with m_{LSP} and so an upper bound on m_{LSP} can be derived from Eq. (19). Note that no lower bound on $\Omega_{\text{LSP}} h^2$ is imposed in our analysis, since the CDM may receive contributions from other particles too [88–92].

Focusing on the HB/FP region, we find that the main processes causing the reduction of $\Omega_{\text{LSP}} h^2$ are the $\tilde{\chi}-\tilde{\chi}$ annihilations (for large $|A_0/M_{1/2}|$'s and low m_{LSP} 's) and the $\tilde{\chi}/\tilde{\chi}_2-\tilde{\chi}_1^+$ coannihilations (for low $|A_0/M_{1/2}|$'s and large m_{LSP} 's). Specifically, the dominant reactions are (see Fig. 1) – the notation used for the various (s)particles is the same as in Table II –

- $\tilde{\chi}\tilde{\chi} \rightarrow W^+W^-$ mediated by a h and H exchange in the s -channel and
- $\tilde{\chi}/\tilde{\chi}_2-\tilde{\chi}_1^+ \rightarrow t\bar{t}$ and $u\bar{d}$ mediated by a $\tilde{b}_{1,2}$ or $\tilde{d}_{L,R}$ exchange in the t -channel, respectively.

Here, as in Sec. IV D, we consider the squarks $\tilde{d}_{L,R}$ of the two lightest generations as degenerate. The strength of the coannihilation processes is controlled by the relative mass splittings $\Delta_{\tilde{\chi}^\pm}$ or $\Delta_{\tilde{\chi}_2}$ between the $\tilde{\chi}_1^+$ or $\tilde{\chi}_2$, respectively, and the LSP, which are defined by

$$\Delta_{\text{CA}} = (m_{\text{CA}} - m_{\text{LSP}})/m_{\text{LSP}}, \quad \text{CA} = \tilde{\chi}^\pm, \tilde{\chi}_2. \quad (20)$$

In particular, we find that the resulting $\Omega_{\text{LSP}} h^2$ decreases with $\Delta_{\tilde{\chi}^\pm}$ or $\Delta_{\tilde{\chi}_2}$. The $\tilde{\chi}/\tilde{\chi}_2-\tilde{\chi}_1^+$ coannihilation processes are dominant in the regions where the bound on $\Omega_{\text{LSP}} h^2$ in Eq. (19) is approached contributing almost 40% to the total effective cross section. On the other hand, in the region where $m_{\tilde{\chi}^\pm}$ is near its lower limit in Eq. (11), the $\tilde{\chi}-\tilde{\chi}$ annihilation processes contribute more than 50% to the reduction of $\Omega_{\text{LSP}} h^2$ – cf. Ref. [30].

2. Spin-independent direct detection of CDM

Direct detection of dark matter through its elastic scattering off atomic nuclei inside an underground detector would be an undeniable evidence of its existence. Data coming from direct detection experiments can provide strict bounds on the values of the free parameters in SUSY models with a sizable higgsino component, as in our case. Here, we focus on the *large underground Xenon* (LUX) experiment [93], whose present data are a little more restrictive than those from the XENON100 experiment [94]. Both belongs to the experiments probing for the *spin-independent* (SI) cross section, since they consider only the scalar part of the cross section. Therefore, the quantity which has to be considered for comparing the experimental results and theoretical predictions is the SI neutralino-proton ($\tilde{\chi} - p$) elastic scattering cross section $\sigma_{\tilde{\chi}p}^{\text{SI}}$. This quantity is calculated by employing the relevant routine of the `micrOMEGAs` package [95] based on the full one-loop treatment of Ref. [96]. The scalar form factors f_{Tq}^p (with $q = u, d, s$) for light quarks in the proton, which are needed for the calculation of $\sigma_{\tilde{\chi}p}^{\text{SI}}$, are estimated following the revised approach of Ref. [97] and taking into account the recent lattice simulations [98], which suggest the following 68% c.l. ranges for the pion-nucleon ($\sigma_{\pi N}$) and the strangeness-nucleon (σ_s) sigma terms:

$$\sigma_{\pi N} = 45 \pm 6 \text{ MeV} \quad \text{and} \quad \sigma_s = 21 \pm 6 \text{ MeV}. \quad (21)$$

Using also as inputs the light quark mass ratios [59] $m_u/m_d = 0.48 \pm 0.1$ and $m_s/m_d = 19.5 \pm 2.5$, we find the following $1 - \sigma$ ranges for the f_{Tq}^p 's:

$$f_{Tu}^p = 0.018_{-0.0044}^{+0.0057}, \quad (22a)$$

$$f_{Td}^p = 0.026_{-0.0019}^{+0.0016}, \quad (22b)$$

$$f_{Ts}^p = 0.022 \pm 0.0064. \quad (22c)$$

Note that these ranges are much narrower than the ones used in Ref. [52]. Also f_{Ts}^p turns out to be considerably smaller than its older value – cf. Ref. [25] – reducing thereby the extracted $\sigma_{\tilde{\chi}p}^{\text{SI}}$.

In the HB/FP region, where the LSP has a significant higgsino component, $\sigma_{\tilde{\chi}p}^{\text{SI}}$ is dominated by the t -channel Higgs-boson-exchange diagram contributing to the neutralino-quark elastic scattering process – for the relevant tree-level interaction terms see e.g. the appendix of Ref. [48]. Especially for large $\tan\beta$'s, which is the case here, the couplings of the heavier Higgs boson H to down-type quarks are proportional to $\tan\beta$ and so are the dominant ones. More explicitly, $\sigma_{\tilde{\chi}p}^{\text{SI}}$ behaves as

$$\sigma_{\tilde{\chi}p}^{\text{SI}} \propto \tan^2\beta |N_{1,1}|^2 |N_{1,3}|^2 / m_H^4, \quad (23)$$

where $N_{1,1}$, $N_{1,2}$, and $N_{1,(3,4)}$ are the elements of the matrix N which diagonalizes the neutralino mass matrix and express the bino, wino, and higgsino component of

$\tilde{\chi}$, respectively. As a consequence, $\sigma_{\tilde{\chi}p}^{\text{SI}}$ can be rather enhanced compared to its value in the $\tilde{\chi} - \tilde{\tau}_1$ coannihilation region, where $\tilde{\chi}$ is essentially a pure bino.

The data from the LUX experiment, which we take from Ref. [99], are directly applicable in the case where the CDM consists of just one kind of weakly interacting massive particle, which in our case would be the neutralino $\tilde{\chi}$. However, if the $\tilde{\chi}$'s constitute only a part of the CDM in the universe, some extra care is required. The number of the scattering events λ is [100–102] proportional to $\sigma_{\tilde{\chi}p}^{\text{SI}}$ and the local $\tilde{\chi}$ density $\rho_{\tilde{\chi}}$:

$$\lambda \propto \sigma_{\tilde{\chi}p}^{\text{SI}} \rho_{\tilde{\chi}}. \quad (24)$$

In the case where the CDM consists only of neutralinos,

$$\rho_{\tilde{\chi}} = \rho_{\text{CDM}}, \quad (25)$$

where ρ_{CDM} is the local CDM density. So, the LUX experiment bound on λ can be directly translated into a bound on $\sigma_{\tilde{\chi}p}^{\text{SI}}$ provided that ρ_{CDM} can be estimated – see e.g. Ref. [103]. However, when the $\tilde{\chi}$'s constitute only a fraction of the total CDM, we can write Eq. (24) as

$$\lambda \propto \sigma_{\tilde{\chi}p}^{\text{SI}} \frac{\rho_{\tilde{\chi}}}{\rho_{\text{CDM}}} \rho_{\text{CDM}}. \quad (26)$$

Following the authors of Ref. [104], we can then use the scaling ansatz

$$\rho_{\tilde{\chi}}/\rho_{\text{CDM}} = \Omega_{\tilde{\chi}}/\Omega_{\text{CDM}}, \quad (27)$$

which gives

$$\lambda \propto \sigma_{\tilde{\chi}p}^{\text{SI}} \frac{\Omega_{\tilde{\chi}}}{\Omega_{\text{CDM}}} \rho_{\text{CDM}}. \quad (28)$$

So, the LUX experiment bound on λ is now translated into a bound on the ‘rescaled’ SI neutralino-proton elastic cross section $\xi\sigma_{\tilde{\chi}p}^{\text{SI}}$, where $\xi = \Omega_{\tilde{\chi}}/\Omega_{\text{CDM}}$.

III. THE HYPERBOLIC BRANCH/FOCUS POINT REGION

A detailed discussion of the characteristics of the HB/FP region of the CMSSM is given in Refs. [26, 27]. The classification of the various solutions of the radiative EWSB condition is based on the expansion of μ^2 in terms of the soft SUSY breaking parameters of the CMSSM included in Eq. (1). Indeed, using fitting techniques, we can verify the following formula

$$\mu^2 + M_Z^2/2 \simeq c_0 m_0^2 + c_{1/2} M_{1/2}^2 + c_A A_0^2 + c_{AM} A_0 M_{1/2}, \quad (29)$$

where the coefficients c_0 , $c_{1/2}$, c_A , and c_{AM} depend basically on $\tan\beta$ and the masses of the fermions of the third generation. These coefficients are computed at the scale M_{SUSY} in Eq. (3) and, therefore, inherit a mild dependence on the SUSY spectrum too. From Eq. (29),

TABLE I: The c 's in Eq. (29) for the four cases of Table II.

$\tan \beta$	c_0	δc_0	$c_{1/2}$	c_A	c_{AM}
40	-0.0921	0.014	0.789	0.107	-0.269
45	-0.0775	0.0148	0.825	0.1016	-0.260
48	-0.0686	0.0151	0.845	0.0981	-0.253
50	-0.0624	0.0265	0.859	0.0953	-0.247

we can easily infer that the SUSY breaking parameters are bounded above for fixed μ , when the quadratic form in the right-hand side of this equation is positive definite. This is the so-called *ellipsoidal branch* (EB). On the contrary, in the *hyperbolic branch* (HB) region [19], c_0 is negative and, consequently, m_0 can become very large together with a combination of A_0 and $M_{1/2}$ with all the other parameters being fixed. Near the boundary between the EB and HB regions, the coefficient c_0 is very close to zero and, thus, m_0 can become very large with all the other parameters fixed. Moreover, there is a region where the soft SUSY breaking mass-squared $m_{H_2}^2$ of H_2 becomes independent of the asymptotic value of the parameter m_0 . This is called the *focus point* (FP) region [22–24].

In the HB region, the radiative EWSB admits three types of solutions [26, 27]:

- (i) Focal Points (HB/FP): They lie near the boundary between the EB and the HB regions, where $c_0 \simeq 0$ and, thus, μ^2 is practically independent of m_0^2 . As a consequence, m_0^2 can become very large, while μ^2 and all the other parameters remain fixed. We should note that, in the large $\tan \beta$ regime, we obtain $\mu^2 + M_Z^2/2 \simeq -m_{H_2}^2$ and so the focal points, where μ^2 is essentially independent of m_0^2 , coincide with the focus points, where $m_{H_2}^2$ is almost m_0^2 -independent. Since, in the present model, $\tan \beta$ is large, we will not distinguish focal from focus points and we will use the same abbreviation (FP) for both.
- (ii) Focal Curves (HB/FC): Along these curves, two of the soft parameters can acquire large values, while μ^2 and all the other parameters remain fixed.
- (iii) Focal Surfaces (HB/FS): Here we can have three soft parameters with large values, while μ^2 and the other parameters remain fixed.

To get an idea of how our solutions in Sec. IV are classified into these categories, we display, in Table I, the values of the coefficients c in Eq. (29) for the four representative cases of Table II corresponding to $\tan \beta = 40, 45, 48,$ and 50 – see Sec. IV D. We also list the relevant $1 - \sigma$ uncertainty δc_0 of c_0 , which is practically the deviation between the lowest c_0 obtained by varying $m_t(m_t)$ in the $1 - \sigma$ range in Eq. (7) and the value of c_0 corresponding to the central value of $m_t(m_t)$ – possible variation of $m_b(M_Z)$ in its $1 - \sigma$ range in Eq. (5) does not change c_0

significantly. As it turns out, the minimal c_0 corresponds to the upper limit of $m_t(m_t)$ in Eq. (7). Taking then the ratio $|c_0|/\delta c_0$, we see that the displacement of c_0 from zero ranges from $2.4 - \sigma$ (for $\tan \beta = 50$) to $6.6 - \sigma$ (for $\tan \beta = 40$). In particular, for $\tan \beta \gtrsim 45$, this displacement does not exceed $5 - \sigma$ and, thus, a real deviation of the coefficient c_0 from zero cannot be established. As a consequence, we can say that the corresponding parameters lie within the HB/FP region. On the contrary, for $\tan \beta \lesssim 45$, the parameters belong to the HB/FC and HB/FS region.

IV. RESTRICTIONS ON THE SUSY PARAMETERS

Imposing the requirements described in Sec. II – with the exception of the one of Sec. II A 5 –, we can restrict the parameters of our model. Following our approach in Refs. [49, 50], we use as free parameters of the model the ones in Eq. (1). The Yukawa coupling constant ratios h_t/h_τ and h_b/h_τ are then fixed by using the data of Sec. II A 1. These ratios must satisfy the YQU conditions in Eq. (2) for natural values of the parameters $\alpha_1, \alpha_2,$ and ρ – see Sec. V. We restrict ourselves to the range $40 \leq \tan \beta \leq 50$ since, below $\tan \beta = 40$, the ratios h_m/h_n ($m, n = t, b, \tau$) tend to require unnatural values of $\alpha_1, \alpha_2,$ and ρ and, above $\tan \beta = 50$, the numerical calculations for the soft SUSY masses become quite unstable. As a characteristic value in our allowed parameter space, we take $\tan \beta = 48$, which balances well enough between maintaining natural values for the h_m/h_n 's and satisfying the various requirements of Sec. II.

We concentrate on the $\mu > 0$ case, given that $\mu < 0$ worsens the violation of Eq. (17a), and scan the region $-30 \leq A_0/M_{1/2} \leq 30$. We will hereafter use the central values of the SM parameters $M_t, m_b(M_Z), m_\tau(M_Z),$ and $\alpha_s(M_Z)$ given in Sec. II A 1. We find that the only constraints which play a role are the lower bound on m_h in Eq. (10), the bounds on $m_{\tilde{\chi}^\pm}$ and $m_{\tilde{g}}$ in Eqs. (11) and (12), the CDM bound in Eq. (19), and the bound from the LUX experiment – see Sec. II B 2. In the parameter space allowed by these requirements, all the other restrictions of Sec. II A are automatically satisfied with the exception of the lower bound on δa_μ in Eq. (17b). This bound is not imposed here as a strict constraint on the parameters of the model for the reasons explained in Sec. II A 5. We only discuss the level at which the requirement in Eq. (17a) is satisfied in the parametric region allowed by all the other constraints.

We first present, in Sec. IV A, the restrictions in the $M_{1/2} - m_0$ plane for low values of $A_0/M_{1/2}$ and then, in Sec. IV B, we reveal the role of the bound in Eq. (12) by considering the $\tan \beta = 48$ case and ignoring the restrictions of Sec. II B 2. In Secs. IV C and IV D, we present regions for various $\tan \beta$'s consistent with all the requirements of Sec. II but the one of Sec. II A 5.

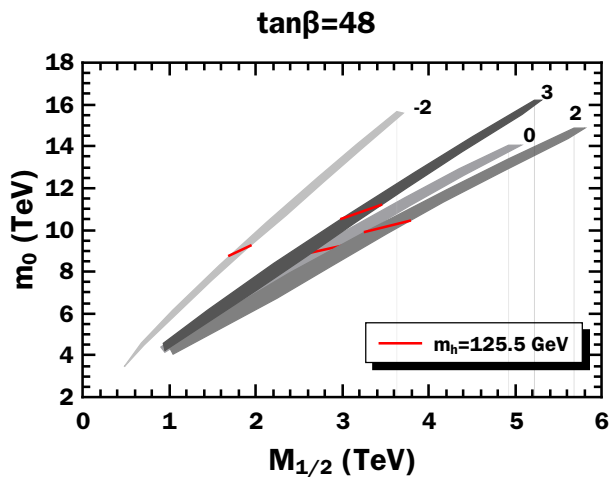


FIG. 2: Allowed (shaded) regions in the $M_{1/2} - m_0$ plane for $\tan\beta = 48$ and different $A_0/M_{1/2}$'s indicated in the plot. The red lines correspond to m_h in Eq. (10).

A. Restrictions in the $M_{1/2} - m_0$ Plane

The interplay of the various requirements of Sec. II can be easily understood from Fig. 2, where we present the (shaded) strips in the $M_{1/2} - m_0$ plane allowed by the restrictions of Secs. II A 1, II A 2, II A 3, II A 4, and II B 1 for $\tan\beta = 48$ and several values of $A_0/M_{1/2}$ indicated in the graph. The upper boundary along each of these allowed strips arises from the limit on $m_{\tilde{\chi}^\pm}$ in Eq. (11). Note that this limit is more restrictive than the limit for triggering radiative EWSB – cf. Ref. [105]. The lower boundary along each strip is given by the upper limit on $\Omega_{\text{LSP}} h^2$ in Eq. (19). On the other hand, the lower limit on m_h in Eq. (9) causes the termination of the strips at low values of m_0 and $M_{1/2}$, whereas their termination at high values of m_0 is put in by hand in order to avoid shifting the SUSY masses to very large values. The red lines indicate solutions with $m_h = 125.5$ GeV – see Eq. (10).

From this figure, we easily see the main features of the HB/FP region: m_0 spans a huge range (4 – 15) TeV, whereas $M_{1/2} [\mu]$ remains relatively low (1 – 6) TeV [(0.1 – 1) TeV] thanks to the structure of the radiative EWSB in this region analyzed in Sec. III. We observe also that as $A_0/M_{1/2}$ increases from -2 to 2 the allowed strip moves to larger $M_{1/2}$'s and becomes less steep, while, for $A_0/M_{1/2} > 2$, we have exactly the opposite behavior: as $A_0/M_{1/2}$ increases, the allowed strip moves to smaller values of $M_{1/2}$ and, at the same time, becomes steeper.

B. Restrictions from the Bound on $m_{\tilde{g}}$

As $|A_0/M_{1/2}|$ increases above 10, the restriction on $m_{\tilde{g}}$ in Eq. (12) comes into play. Its importance can be easily inferred from Fig. 3, where we plot $m_{\tilde{g}}$ against $A_0/M_{1/2}$ for m_h as in Eq. (10) and $\tan\beta = 48$ – let us

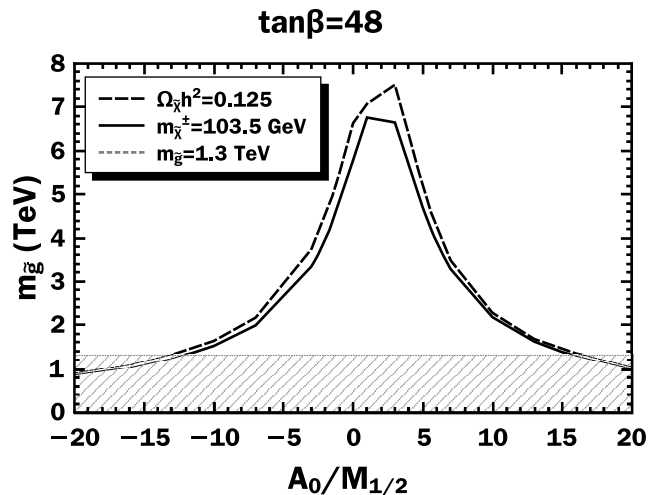


FIG. 3: Restrictions in the $A_0/M_{1/2} - m_{\tilde{g}}$ plane from Eq. (11) (solid line) and Eq. (19) (dashed line) for m_h in Eq. (10) and $\tan\beta = 48$. The region excluded by Eq. (12) is cross hatched.

note that varying $\tan\beta$ does not significantly affect this figure. The solid [dashed] line corresponds to the limit on $m_{\tilde{\chi}^\pm}$ [$\Omega_{\text{LSP}} h^2$] in Eq. (11) [Eq. (19)]. The dotted line denotes the lower limit on $m_{\tilde{g}}$ in Eq. (12) excluding the cross hatched region. Therefore, the allowed region (still without considering the LUX data – see Sec. II B 2) is the region bounded by the three aforementioned lines. We see clearly that the bound on $m_{\tilde{g}}$ cuts off the largest values of $|A_0/M_{1/2}|$. Specifically, near the lower bound on $m_{\tilde{\chi}^\pm}$ given in Eq. (11), $A_0/M_{1/2}$ is limited in the range $-10.8 \lesssim A_0/M_{1/2} \lesssim 14.4$, while, near the upper bound on $\Omega_{\text{LSP}} h^2$ in Eq. (19), it is limited in the range $-11.7 \lesssim A_0/M_{1/2} \lesssim 15.5$. In order to understand this behavior, let us recall that m_h depends on the ratio $X_t^2/m_{\tilde{t}}^2$, where $X_t = A_t - \mu \cot\beta$ with A_t being the soft trilinear scalar coupling constant for the t -squark. For m_h and $\tan\beta$ fixed, we see that larger absolute values of $A_0/M_{1/2}$ require larger $m_{\tilde{t}}$'s too and, since $m_{\tilde{t}}$ depends largely on m_0 , the latter must grow larger as well together with the left-handed squark soft SUSY breaking masses M_{QL} . These soft masses increase as the soft gluino mass M_3 decreases – see the relevant renormalization group equation in Ref. [7] – and, thus, it is quite obvious that, in order to achieve larger values of M_{QL} , we need smaller M_3 's, which also suggests smaller values for the common asymptotic gaugino mass $M_{1/2}$. Therefore, small $M_{1/2}$'s and large $|A_0|$'s, which lead to big $|A_0/M_{1/2}|$'s, yield small $m_{\tilde{g}}$'s, which is exactly what one deduces from Fig. 3.

C. Restrictions from the LUX Experiment

Considering the cross section $\sigma_{\tilde{\chi} p}^{\text{SI}}$, we can not only probe the detectability of the LSP, but also obtain further restrictions on the parameters of our model. This

is because of the rather enhanced $\sigma_{\tilde{\chi}p}^{\text{SI}}$'s obtained in the HB/FP region, as explained in Sec. II B 2. In the computation of $\sigma_{\tilde{\chi}p}^{\text{SI}}$, we adopt the central values of the f_{Tq}^p 's in Eqs. (22a)-(22c) and fix m_h to its value in Eq. (10). The results are presented in Fig. 4, where we depict the allowed (bounded) regions in the $m_{\text{LSP}} - \xi\sigma_{\tilde{\chi}p}^{\text{SI}}$ plane for $\tan\beta = 40$ (upper panels) $\tan\beta = 48$ (middle panels) and $\tan\beta = 50$ (lower panels). We also draw with gray solid and dashed lines the projected sensitivities [99] of the XENON1T [106] and LUX-ZEPLIN [107] experiments, respectively. The panels in the left [right] column correspond to $A_0/M_{1/2} \leq 0$ [$A_0/M_{1/2} \geq 0$]. We see that, for each $\tan\beta$, the allowed regions in the left and right panel almost coincide and, thus, we display them separately to avoid confusion. The numbers on the various points of each boundary line indicate the corresponding values of $A_0/M_{1/2}$.

The allowed regions are bounded by five different types of black lines for which we adopt the following conventions:

- on the solid line the bound on $m_{\tilde{\chi}\pm}$ coming from Eq. (11) is saturated;
- on the double dot-dashed line the limit on $m_{\tilde{g}}$ in Eq. (12) is saturated;
- on the dashed line the bound on $\Omega_{\text{LSP}}h^2$ from Eq. (19) is saturated;
- the dotted line depicts the bound on $\xi\sigma_{\tilde{\chi}p}^{\text{SI}}$ arising from the LUX data taken from Ref. [99];
- the dash-dotted line represents the lowest possible $\sigma_{\tilde{\chi}p}^{\text{SI}}$ in each case.

As can be understood from the description of the various lines above, we have $\xi = 1$ along the dashed line. As regards the minimal ξ , this reaches 0.013 independently of $\tan\beta$.

Notice that there are no significant differences between the various $\tan\beta$'s as regards the allowed ranges of m_{LSP} and $A_0/M_{1/2}$. From all these graphs, we deduce that, as we move towards the $\Omega_{\text{LSP}}h^2 = 0.125$ line, m_{LSP} and $m_{\tilde{\chi}\pm}$ grow larger, while the allowed range of $A_0/M_{1/2}$ becomes smaller. The largest $|A_0/M_{1/2}|$ is located at the junction point of the double dot-dashed and dotted lines – with the exception of the allowed region for $\tan\beta = 50$ and $A_0/M_{1/2} > 0$, where the largest $|A_0/M_{1/2}|$ is found at the intersection of the solid and double dot-dashed lines. The smallest m_{LSP} can be found in the upper left corner of the allowed regions, whereas the largest m_{LSP} is found on the dashed line. The allowed ranges of $A_0/M_{1/2}$ and m_{LSP} can be summarized as follows:

- For $\tan\beta = 40$, we find $-12.4 \lesssim A_0/M_{1/2} \lesssim 16.28$ and $92 \lesssim m_{\text{LSP}}/\text{GeV} \lesssim 1084.8$.
- For $\tan\beta = 48$, we find $-12.8 \lesssim A_0/M_{1/2} \lesssim 15.8$ and $92 \lesssim m_{\text{LSP}}/\text{GeV} \lesssim 1084.2$.

- For $\tan\beta = 50$, we find $-13 \lesssim A_0/M_{1/2} \lesssim 15.35$ and $91.9 \lesssim m_{\text{LSP}}/\text{GeV} \lesssim 1088$.

We noticed that, as $A_0/M_{1/2}$ approaches 2 from above, the value of the product $|N_{1,1}|^2|N_{1,3}|^2$ decreases. However, as $A_0/M_{1/2}$ decreases below 2, $|N_{1,1}|^2|N_{1,3}|^2$ grows. The growth of this product persists even when $A_0/M_{1/2}$ becomes negative. As a consequence – see Eq. (23) – $\xi\sigma_{\tilde{\chi}p}^{\text{SI}}$ acquires its minimal value at $A_0/M_{1/2} = 2$. The overall minimum of $\xi\sigma_{\tilde{\chi}p}^{\text{SI}}$, for each value of $\tan\beta$, is acquired at the lowest left corner of the corresponding allowed region in the right column of Fig. 4. The smallest of these overall minima, for $\tan\beta \geq 40$, is

$$\xi\sigma_{\tilde{\chi}p}^{\text{SI}} \gtrsim 1.56 \times 10^{-12} \text{ pb} \quad (1.49 \times 10^{-12} \text{ pb}), \quad (30)$$

and it is obtained at $\tan\beta = 40$ and $m_{\text{LSP}} \simeq 101.7 \text{ GeV}$. The bound in parenthesis is derived by allowing the f_{Tq}^p 's to vary within their $1 - \sigma$ intervals in Eqs. (22a), (22b), and (22c). As shown in the plots, the obtained values of $\xi\sigma_{\tilde{\chi}p}^{\text{SI}}$ are within the reach of forthcoming experiments like XENON1T and LUX-ZEPLIN with planned sensitivity from 10^{-45} to 10^{-47} cm^2 for the m_{LSP} range under consideration – recall that $1 \text{ pb} = 10^{-36} \text{ cm}^2$.

D. The Overall Allowed Parameter Space

In order to have a more spherical view of the allowed parameter space of our model, we present in Fig. 5 the allowed regions in the $m_A - A_0/M_{1/2}$ plane for $\tan\beta = 40, 48$, and 50 enclosed by blue, red, and green lines, respectively. As one can see from Fig. 4 and the allowed ranges of m_{LSP} presented in Sec. IV C, the mass of the LSP (and $M_{1/2}$) is confined in approximately the same range independently of $\tan\beta$. Therefore, we opt to use m_A as variable in the horizontal axis, so that the allowed regions corresponding to different $\tan\beta$'s are well distinguishable. We observe that, although the range of m_{LSP} is practically $\tan\beta$ -independent, m_A increases as $\tan\beta$ decreases. For each value of $\tan\beta$, there are three different boundary lines corresponding to different restrictions. On the solid and dashed line, the bounds on $m_{\tilde{\chi}\pm}$ in Eq. (11) and on $\Omega_{\text{LSP}}h^2$ in Eq. (19) are saturated, whereas the restriction from the LUX data on $\xi\sigma_{\tilde{\chi}p}^{\text{SI}}$ yields the dotted boundary line. It is impressive that the LUX data provide such a strong constraint on the model parameters, which overshadows all other constraints for approximately $A_0/M_{1/2} \lesssim -3$ and $A_0/M_{1/2} \gtrsim 5$. Finally, the boundary lines from the limit on $m_{\tilde{g}}$ in Eq. (12), although hardly visible in this plot, provide the maximal and minimal $A_0/M_{1/2}$'s. Note that the allowed regions are obviously symmetric about $A_0/M_{1/2} \simeq 2.5$. Also, we find that μ remains almost constant $\simeq 100 \pm 20 \text{ GeV}$ on the solid lines from Eq. (11), while it reaches about 1 TeV when the bound in Eq. (19) is saturated. As regards δa_μ , the acquired values are well below the lower limit in Eq. (17b). Specifically, in the allowed regions of

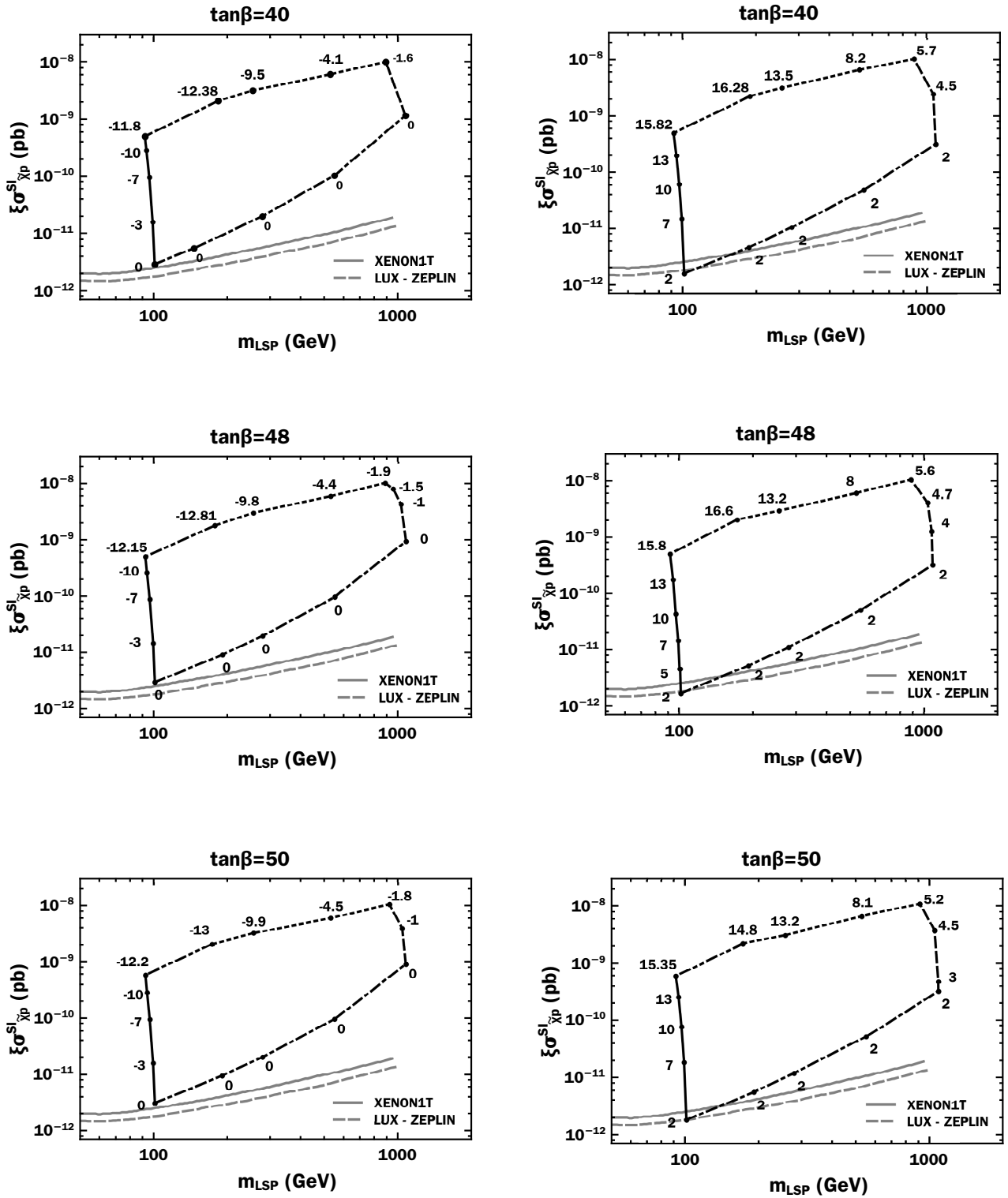


FIG. 4: Allowed (bounded) regions in the $m_{\text{LSP}} - \xi \sigma_{\chi p}^{\text{SI}}$ plane for m_h given by Eq. (10) and $\tan\beta = 40, 48$, and 50 . The left [right] panels correspond to $A_0/M_{1/2} \leq 0$ [$A_0/M_{1/2} \geq 0$] and the values of $A_0/M_{1/2}$ at the various points of the boundary lines are indicated. The black solid, double dot-dashed, and dashed lines correspond to the bounds from Eqs. (11), (12), and (19), respectively. The black dotted lines arise from the LUX data, whereas the black dot-dashed lines give the lowest possible $\xi \sigma_{\chi p}^{\text{SI}}$ in each case. The planned sensitivity limits of XENON1T and LUX-ZEPLIN are also depicted by a gray solid and dashed line, respectively.

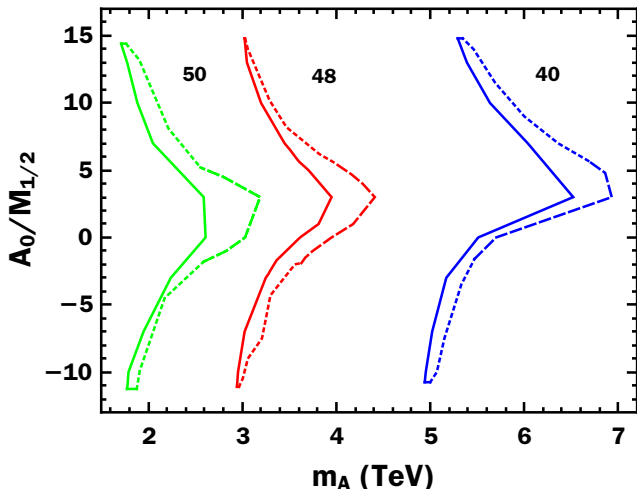


FIG. 5: Allowed regions in the $m_A - A_0/M_{1/2}$ plane with m_h given by Eq. (10) and for $\tan\beta = 40, 48,$ and 50 , bounded by blue, red, and green lines, respectively. The solid, dashed, and dotted boundary lines come from the constraints in Eqs. (11), (19), and the LUX data, respectively. The restriction in Eq. (12) limits the range of $A_0/M_{1/2}$, but the corresponding lines are hardly visible.

Fig. 5, we obtain $\delta a_\mu \simeq (0.04 - 0.27) \times 10^{-10}$. Therefore, Eq. (17a) is satisfied only at the level of 2.83 to $2.86 - \sigma$.

The values of the input and some output parameters, the mass spectra and some low energy observables of the model are listed in Table II for four characteristic points of the allowed parameter space with $m_h = 125.5$ GeV. The various masses of the SUSY particles (gauginos/higgsinos $\tilde{\chi}, \tilde{\chi}_2, \tilde{\chi}_3, \tilde{\chi}_4, \tilde{\chi}_1^\pm, \tilde{\chi}_2^\pm, \tilde{g}$, squarks $\tilde{t}_1, \tilde{t}_2, \tilde{b}_1, \tilde{b}_2, \tilde{u}_L, \tilde{u}_R, \tilde{d}_L, \tilde{d}_R$, and sleptons $\tilde{\tau}_1, \tilde{\tau}_2, \tilde{\nu}_\tau, \tilde{e}_L, \tilde{e}_R$) and the Higgs particles (h, H, H^\pm, A) are given in TeV – note that we consider the first two generations of squarks and sleptons as degenerate. We chose the values of the input parameters so as to assure that $\Omega_{\text{LSP}} h^2$ is not far from its central value in Eq. (18). The relatively low $\Delta_{\tilde{\chi}^\pm}$'s and $\Delta_{\tilde{\chi}_2}$'s obtained and the sizable higgsino fraction $|N_{1,3}|^2 + |N_{1,4}|^2$ assist us to achieve this. Note that, in all the cases, the lightest neutralino mass turns out to be close to the corresponding μ . We also include an estimate for the EWSB fine-tuning parameter Δ_{EW} – see Sec. VI.

We observe that the low energy B -physics observables satisfy the relevant constraints in Sec. II A 4, whereas the δa_μ 's are far below the lower limit in Eq. (17b). Also, the extracted $\sigma_{\tilde{\chi}p}^{\text{SI}}$'s can be probed by the forthcoming experiments [106, 107]. For the spin-dependent $\tilde{\chi} - p$ scattering cross section $\sigma_{\tilde{\chi}p}^{\text{SD}}$, we adopt the central values for the hadronic inputs in Ref. [52]. As can be easily deduced from the displayed values, $\sigma_{\tilde{\chi}p}^{\text{SD}}$ in our model lies well below the sensitivity of IceCube [108] (assuming $\tilde{\chi} - \tilde{\chi}$ annihilation into W^+W^-) and the expected limit from the large DMTPC detector [99]. Therefore, the LSPs

predicted by our model can be detectable only by the future experiments which will release data on $\sigma_{\tilde{\chi}p}^{\text{SI}}$.

Comparing the results of Table II with the corresponding ones in the $\tilde{\chi} - \tilde{\tau}_1$ coannihilation region – see Table II of Refs. [49, 50] –, we may appreciate the different features of the HB/FP solutions presented here. First of all, m_0 acquires considerably larger values here, while μ remains quite small. The Higgs bosons $H, H^\pm,$ and A acquire larger masses and the whole sparticle spectrum, with the exception of the neutralinos and charginos, becomes heavier. The gluino mass is heavier for lower $\tan\beta$'s, in contrast with what happens in the $\tilde{\chi} - \tilde{\tau}_1$ coannihilation region, where we observe the opposite behavior. Here, the ratio h_b/h_τ is smaller, h_t/h_b is closer to 2, while h_t/h_τ is even closer to unity. The restrictions on the low energy observables are all well satisfied, except the one on δa_μ , which becomes even smaller than in the $\tilde{\chi} - \tilde{\tau}_1$ coannihilation region. Note that the latter region is tightly constrained by $\text{BR}(B_s \rightarrow \mu^+\mu^-)$, which is well suppressed in the HB/FP region. As regards $\Omega_{\text{LSP}} h^2$, this becomes compatible with Eq. (19) in the present case thanks to $\tilde{\chi}/\tilde{\chi}_2 - \tilde{\chi}_1^+$ coannihilations, which are activated because of the low $\Delta_{\tilde{\chi}^\pm}$'s and $\Delta_{\tilde{\chi}_2}$'s. Note that, in the $\tilde{\chi} - \tilde{\tau}_1$ coannihilation region, the relevant mass splittings are $\Delta_{\tilde{\tau}_1} = (m_{\tilde{\tau}_1} - m_{\text{LSP}})/m_{\text{LSP}}$ and $\Delta_H = (m_H - 2m_{\text{LSP}})/2m_{\text{LSP}}$. Finally, here we obtain a large higgsino fraction of the LSP, which confines m_{LSP} close to μ and as a bonus ensures $\sigma_{\tilde{\chi}p}^{\text{SI}}$'s accessible to the forthcoming experiments [106, 107]. On the contrary, within the $\tilde{\chi} - \tilde{\tau}_1$ coannihilation region, $\tilde{\chi}$ is an almost pure bino, $m_{\text{LSP}} \simeq M_{1/2}/2$, and $\sigma_{\tilde{\chi}p}^{\text{SI}}$ is well below the sensitivity of any planned experiment.

V. DEVIATION FROM YUKAWA UNIFICATION

The ranges of the ratios of the asymptotic third generation Yukawa coupling constants in the allowed parameter space of the model in the range $40 \leq \tan\beta \leq 50$, which we consider here, are the following:

$$1 \lesssim \frac{h_t}{h_\tau} \lesssim 1.5, \quad 0.75 \lesssim \frac{h_b}{h_\tau} \lesssim 0.79, \quad \text{and} \quad 1.2 \lesssim \frac{h_t}{h_b} \lesssim 2. \quad (31)$$

It is easy to see that, although YU is violated, these ratios turn out to be quite close to unity. However, for $\tan\beta < 40$, the ratios h_t/h_τ and h_t/h_b become large and the term ‘Yukawa quasi-unification conditions’ cannot be justified for the constraints given in Eq. (2). So, we restrict ourselves to $\tan\beta \geq 40$.

We will now give a specific example of how such values for the ratios of the Yukawa coupling constants as the ones in Eq. (31) can be achieved in a natural way. We consider the third case in Table II with $\tan\beta = 48$, where $h_t/h_\tau = 1.107$ and $h_b/h_\tau = 0.763$, and solve Eq. (2) with respect to the complex parameters α_1, α_2 , and the real and positive parameter ρ . Specifically, we first find pairs of values for ρ and α_1 which satisfy the YQU condition

TABLE II: Input/output parameters, sparticle and Higgs masses, and low energy observables in four cases in the HB/FP.

Input parameters				
$\tan \beta$	40	45	48	50
$A_0/M_{1/2}$	2	0	-1.5	-3
$M_{1/2}/\text{TeV}$	3.763	2.945	2.161	1612.4
m_0/TeV	9.603	8.821	9.231	9.561
Output parameters				
$h_t/h_\tau(M_{\text{GUT}})$	1.474	1.237	1.107	1.027
$h_b/h_\tau(M_{\text{GUT}})$	0.756	0.758	0.763	0.774
$h_t/h_b(M_{\text{GUT}})$	1.949	1.631	1.45	1.326
μ/TeV	1.018	1.01	0.928	0.736
$\Delta_{\tilde{\chi}^\pm}$	0.002	0.004	0.014	0.038
$\Delta_{\tilde{\chi}_2}$	0.004	0.006	0.018	0.045
Δ_{EW}	244.6	237.9	216.2	130.9
$ N_{1,3} ^2 + N_{1,4} ^2$	0.997	0.992	0.836	0.54
Sparticle and Higgs boson masses in TeV				
$\tilde{\chi}, \tilde{\chi}_2$	1.043, 1.047	1.026, 1.032	0.935, 0.952	0.723, 0.756
$\tilde{\chi}_3, \tilde{\chi}_4$	1.792, 3.381	1.397, 2.651	1.034, 1.959	0.788, 1.473
$\tilde{\chi}_1^\pm, \tilde{\chi}_2^\pm$	1.046, 3.381	1.030, 2.651	0.949, 1.959	0.751, 1.473
\tilde{g}	8.147	6.512	4.951	3.799
\tilde{t}_1, \tilde{t}_2	8.113, 9.516	6.900, 7.984	6.309, 7.270	6.049, 6.900
\tilde{b}_1, \tilde{b}_2	9.515, 10.23	7.987, 8.560	7.267, 7.887	6.897, 7.512
\tilde{u}_L, \tilde{u}_R	11.777, 11.553	10.357, 10.197	10.100, 10.004	10.082, 10.022
\tilde{d}_L, \tilde{d}_R	11.777, 11.524	10.357, 10.176	10.100, 9.992	10.082, 10.014
$\tilde{\tau}_1, \tilde{\tau}_2$	7.927, 9.104	6.921, 8.136	6.749, 8.202	6.620, 8.292
$\tilde{\nu}_\tau$	9.103	8.135	8.201	8.291
\tilde{e}_L, \tilde{e}_R	9.936, 9.718	9.050, 8.900	9.359, 9.276	9.640, 9.589
$\tilde{\nu}_e$	9.935	9.049	9.359	9.639
h, H	0.1255, 6.56	0.1255, 4.820	0.1255, 3.67	0.1255, 2.369
H^\pm, A	6.56, 6.56	4.820, 4.820	3.671, 3.67	2.370, 2.371
Low energy observables				
$10^4 \text{BR}(b \rightarrow s\gamma)$	3.31	3.30	3.30	3.33
$10^9 \text{BR}(B_s \rightarrow \mu^+ \mu^-)$	3.04	3.03	3.02	2.97
$R(B_u \rightarrow \tau \nu)$	0.998	0.995	0.991	0.976
$10^{10} \delta a_\mu$	0.135	0.2	0.227	0.237
$\Omega_{\text{LSP}} h^2$	0.11	0.11	0.11	0.11
$\sigma_{\tilde{\chi}_p^{\text{SI}}}/10^{-9} \text{pb}$	0.28	0.81	7.75	13.29
$\sigma_{\tilde{\chi}_p^{\text{SD}}}/10^{-7} \text{pb}$	2.55	7.87	77.08	227.8

for h_b/h_τ and, then, for each one of these pairs, we find α_2 's which satisfy the equation for h_t/h_τ . Note that, while h_b/h_τ depends only on the value of the product $\rho\alpha_1$, the ratio h_t/h_τ depends on each of the parameters α_1 , α_2 , and ρ separately. This is the reason why the solutions in the α_1 complex plane lie on a set of similar curves corresponding to different values of ρ , whereas the values of α_2 do not follow any specific pattern in the corresponding complex plane – see below. We found that solutions exist only for low values of ρ (up to about 0.6) and also for large values of this parameter ($\rho \gtrsim 2.4$).

We present several of these solutions in the α_1 and α_2 complex planes in Fig. 6, but only for the lower values of ρ , which are considered more natural. In the left panel

of this figure, we see that, for any given value of ρ , the data clearly lie on a specific curve and that the curves for different values of ρ are similar to each other. On the other hand, in the right panel, the data are more complicatedly distributed. Note that, every pair of values of α_1 and ρ corresponds to more than one value of α_2 . From Fig. 6, we can deduce that, for the specific example considered and for small values of ρ , the ranges of the values of all the parameters are the following:

$$0.3 \lesssim \rho \lesssim 0.5, \quad (32a)$$

$$-0.45 \lesssim \text{Re}(\alpha_1) \lesssim 0.31, \quad 0.95 \lesssim \text{Im}(\alpha_1) \lesssim 2.19, \quad (32b)$$

$$-1.39 \lesssim \text{Re}(\alpha_2) \lesssim 0.83, \quad 0.01 \lesssim \text{Im}(\alpha_2) \lesssim 1.21. \quad (32c)$$

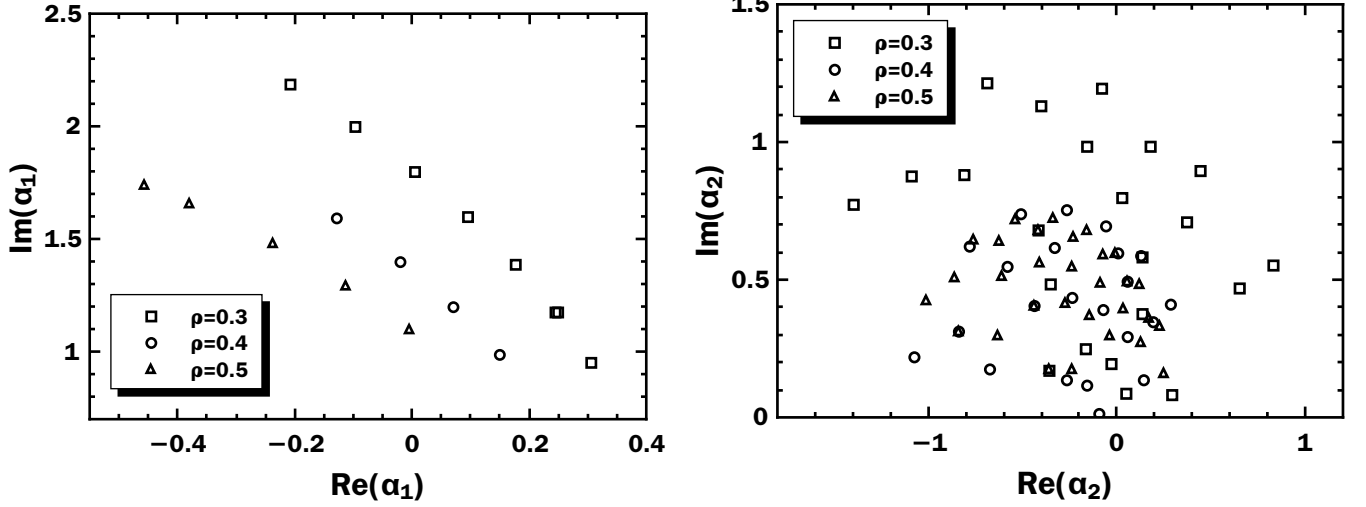


FIG. 6: The complex parameters α_1 and α_2 for various real and positive values of ρ indicated on the graphs for the case in the third column of Table II with $\tan\beta = 48$.

Note also that, for the larger values of ρ , we get smaller values for α_1 and α_2 . So, we see that the ratios of the Yukawa coupling constants in this example can be easily obtained by natural choices of ρ , α_1 , and α_2 .

We find that, for all the possible values of the ratios of the third generation Yukawa coupling constants encountered in our investigation, the picture is quite similar. So, we conclude that these ratios can be readily obtained by a multitude of natural choices of the parameters ρ , α_1 , and α_2 everywhere in the allowed parameter space of the model which we considered here.

VI. NATURALNESS OF THE EWSB

One of the most important reasons for introducing SUSY was that it could provide a solution to the hierarchy problem. However, the fact that, in our model, m_0 turns out to lie in the multi-TeV range generates doubts about the naturalness of the radiative EWSB, since it leads to the reappearance of a small fine-tuning problem. This is the so-called *little hierarchy problem*, which is still a much debated issue.

To quantify somehow the naturalness of our model with respect to this issue, we focus on the EWSB condition relating M_Z to μ and $\tan\beta$. This condition is obtained by minimizing the tree-level renormalization-group improved scalar potential for H_1 and H_2 and reads as follows [7]

$$\frac{1}{2}M_Z^2 \simeq \frac{m_{H_1}^2 - m_{H_2}^2 \tan^2\beta}{\tan^2\beta - 1} - \mu^2, \quad (33)$$

where m_{H_1} is the soft SUSY breaking mass of H_1 and we neglect possible loop corrections, which are anyway

minimized thanks to the choice of the optimal scale in Eq. (3). In the case where the value of the fraction in the right-hand side of Eq. (33) is quite large, a large value of μ^2 is also needed. However, this requires large values of m_0 and $M_{1/2}$ and heavy sparticle spectrum and, therefore, introduces a certain amount of fine-tuning. To measure this tuning, we introduce the EWSB fine-tuning parameter

$$\Delta_{\text{EW}} \equiv \max\left(\frac{|C_i|}{M_Z^2/2}\right), \quad (34)$$

where the C_i 's ($i = \mu, H_1, H_2$) are – see Eq. (33) – :

$$(C_\mu, C_{H_1}, C_{H_2}) = \left(-\mu^2, \frac{m_{H_1}^2}{\tan^2\beta - 1}, -\frac{m_{H_2}^2 \tan^2\beta}{\tan^2\beta - 1}\right). \quad (35)$$

In most of the parameter space explored, Δ_{EW} is dominated by the term C_μ .

Focusing on the values of the parameters which ensure $\Omega_{\text{LSP}} h^2 = 0.125$, we present, in the left panel of Fig. 7, $M_{1/2}$ (solid line) and Δ_{EW} (dashed line) as functions of m_{LSP} for $\tan\beta = 48$, $m_h = 125.5$ GeV, and negative values of $A_0/M_{1/2}$ indicated in the graph – cf. the left panel in Fig. 4 for $\tan\beta = 48$. We clearly see that the required EWSB fine-tuning parameter Δ_{EW} is almost constant and ~ 200 . This result is also valid for the other two values of $\tan\beta$ in Fig. 4. Indeed, for the largest value of $|A_0/M_{1/2}|$ on the dashed line in each of the six panels of Fig. 4, the derived Δ_{EW} is as follows:

- For $\tan\beta = 40$ and $A_0/M_{1/2} = -1.6$ [$A_0/M_{1/2} = 5.7$], we find $\Delta_{\text{EW}} = 191.311$ [$\Delta_{\text{EW}} = 187.379$].
- For $\tan\beta = 48$ and $A_0/M_{1/2} = -1.9$ [$A_0/M_{1/2} = 5.6$], we find $\Delta_{\text{EW}} = 188.064$ [$\Delta_{\text{EW}} = 187.724$].

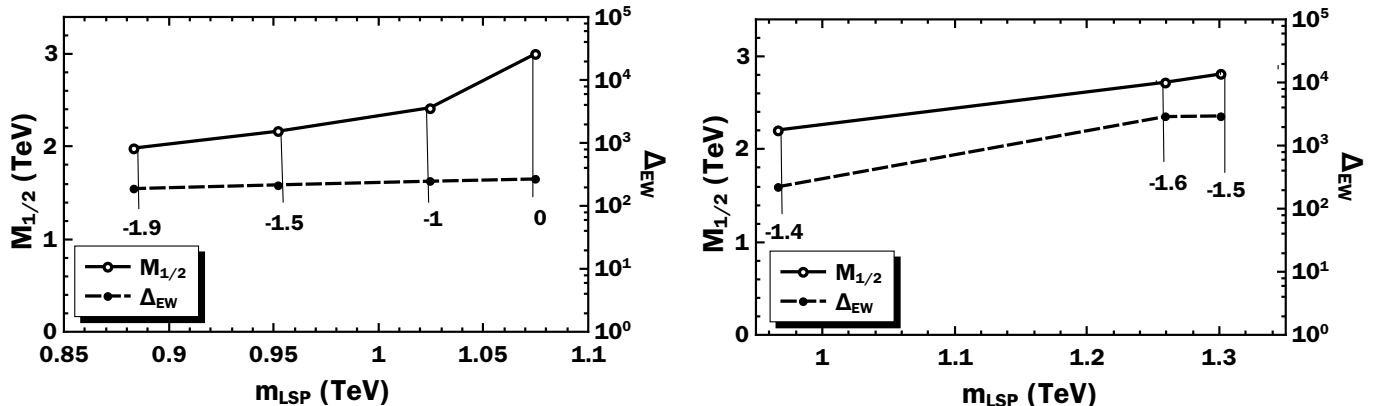


FIG. 7: $M_{1/2}$ and Δ_{EW} as functions of m_{LSP} for $\Omega_{LSP} h^2 = 0.125$, m_h given by Eq. (10) and various $A_0/M_{1/2}$'s indicated on the curves for the HB/FP (left panel) and the $\tilde{\chi} - \tilde{\tau}_1$ coannihilation (right panel) region of the model.

- For $\tan \beta = 50$ and $A_0/M_{1/2} = -1.8$ [$A_0/M_{1/2} = 5.2$], we find $\Delta_{EW} = 204.702$ [$\Delta_{EW} = 201.228$].

The value of Δ_{EW} can be even smaller for lower m_{LSP} 's and $\Omega_{LSP} h^2$'s. However, we believe that the values presented above are more interesting, especially if we wish to compare the Δ_{EW} 's found in the HB/FP region with the ones in the $\tilde{\chi} - \tilde{\tau}_1$ coannihilation region analyzed in Ref. [50]. To this end, we plot also, in the right panel of Fig. 7, $M_{1/2}$ (solid line) and Δ_{EW} (dashed line) as functions of m_{LSP} in the $\tilde{\chi} - \tilde{\tau}_1$ coannihilation region of the same model for $\tan \beta = 48$, $m_h = 125.5$ GeV, and $A_0/M_{1/2} < 0$ – see Fig. 3 of Ref. [50]. It is evident that, in this coannihilation region, the required values of m_{LSP} are somewhat larger and the values of Δ_{EW} can become about a factor of ten larger ($\Delta_{EW} > 1000$). We can, thus, easily appreciate the amelioration regarding the EWSB fine-tuning that we achieve working in the HB/FP region.

VII. CONCLUSIONS

We investigated the compatibility of the generalized asymptotic Yukawa coupling constant quasi-unification, which yields acceptable masses for the fermions of the third family, with the HB/FP region of the CMSSM for $\mu > 0$ and $40 \leq \tan \beta \leq 50$. We imposed phenomenological constraints originating from the mass of the lightest neutral CP-even Higgs boson, the lower bounds on the masses of the sparticles, and B -physics. We also considered cosmological constraints coming from the CDM relic abundance in the universe and the LUX data on

the spin-independent neutralino-proton elastic scattering cross section. Fixing m_h to its central value favored by the LHC, we found a relatively wide allowed range of parameters with $-11 \lesssim A_0/M_{1/2} \lesssim 15$ and $0.09 \lesssim m_{LSP}/\text{TeV} \lesssim 1.1$. The restriction on the deviation of the measured value of the muon anomalous magnetic moment from its SM prediction, however, is only satisfied at the level of about $2.8 - \sigma$ in this parameter space allowed by all the other requirements.

The LSP, which is a bino-higgsino admixture, has an acceptable relic abundance thanks to coannihilations between the LSP and the next-to-lightest neutralino with the lightest chargino. The LSP is also possibly detectable in the planned CDM direct search experiments which look for the spin-independent elastic cross section between neutralino and proton. The required deviation from YU can be easily attributed to a multitude of natural values of the relevant parameters within a Pati-Salam SUSY GUT model and the EWSB fine-tuning Δ_{EW}^{-1} turns out to be of the order of 5×10^{-3} . It is worth mentioning that the same model has been tested successfully in the $\tilde{\chi} - \tilde{\tau}_1$ coannihilation region [50]. However, the allowed parametric space turned out to be much more restricted there, the detectability of the LSP quite difficult, and the EWSB fine-tuning worse.

Acknowledgements We would like to thank B.E. Allanach and D. George in DAMTP, Cambridge as well as N. Mavromatos in King's College, London for useful discussions. This research was supported from the MEC and FEDER (EC) grants FPA2011-23596 and the Generalitat Valenciana under grant PROMETEOII/2013/017.

[1] A. Chamseddine, R. Arnowitt, and P. Nath, Phys. Rev. Lett. **49**, 970 (1982).
 [2] P. Nath, R. Arnowitt, and A. Chamseddine, Nucl. Phys.

B **227**, 121 (1983).
 [3] N. Ohta, Prog. Theor. Phys. **70**, 542 (1983).
 [4] L. Hall, J. Lykken, and S. Weinberg, Phys. Rev. D **27**,

- 2359 (1983).
- [5] R. Arnowitt and P. Nath, *Phys. Rev. Lett.* **69**, 725 (1992).
- [6] G. Ross and R. Roberts, *Nucl. Phys. B* **377**, 571 (1992).
- [7] V. Barger, M. Berger, and P. Ohmann, *Phys. Rev. D* **49**, 4908 (1994).
- [8] G. Kane, C. Kolda, L. Roszkowski, and J. Wells, *Phys. Rev. D* **49**, 6173 (1994).
- [9] G. Aad et al. (ATLAS Collaboration), *Phys. Rev. D* **90**, 052004 (2014).
- [10] CMS Collaboration, Tech. Rep. CMS-PAS-HIG-14-009 (2014).
- [11] R. Aaij et al. (LHCb Collaboration), *Phys. Rev. Lett.* **108**, 231801 (2012).
- [12] J. Albrecht, *Mod. Phys. Lett. A* **27**, 1230028 (2012).
- [13] R. Aaij et al. (LHCb Collaboration), *Phys. Rev. Lett.* **110**, 021801 (2013).
- [14] P. Ade et al. (Planck Collaboration), *Astron. Astrophys.* **571**, A16 (2014).
- [15] J. Ellis and K. Olive, *Eur. Phys. J. C* **72**, 2005 (2012).
- [16] H. Baer, V. Barger, P. Huang, and X. Tata, *J. High Energy Phys.* **05**, 109 (2012).
- [17] O. Buchmueller et al., *Eur. Phys. J. C* **74**, 2922 (2014).
- [18] L. Roszkowski, E. M. Sessolo, and A. J. Williams, *J. High Energy Phys.* **08**, 067 (2014).
- [19] K. Chan, U. Chattopadhyay, and P. Nath, *Phys. Rev. D* **58**, 096004 (1998).
- [20] H. Baer, C.-h. Chen, C. Kao, and X. Tata, *Phys. Rev. D* **52**, 1565 (1995).
- [21] K. L. Chan, U. Chattopadhyay, and P. Nath, *Phys. Rev. D* **58**, 096004 (1998).
- [22] J. L. Feng, K. T. Matchev, and T. Moroi, *Phys. Rev. Lett.* **84**, 2322 (2000).
- [23] J. L. Feng and D. Sanford, *Phys. Rev. D* **86**, 055015 (2012).
- [24] A. Delgado, M. Quiros, and C. Wagner, *J. High Energy Phys.* **04**, 093 (2014).
- [25] P. Draper, J. L. Feng, P. Kant, S. Profumo, and D. Sanford, *Phys. Rev. D* **88**, 015025 (2013).
- [26] S. Akula, M. Liu, P. Nath, and G. Peim, *Phys. Lett. B* **709**, 192 (2012).
- [27] M. Liu and P. Nath, *Phys. Rev. D* **87**, 095012 (2013).
- [28] H. Baer, C. Balazs, and A. Belyaev, *J. High Energy Phys.* **03**, 042 (2002).
- [29] J. Edsjo, M. Schelke, P. Ullio, and P. Gondolo, *J. Cosmol. Astropart. Phys.* **04**, 001 (2003).
- [30] B. Allanach, G. Belanger, F. Boudjema, and A. Pukhov, *J. High Energy Phys.* **12**, 020 (2004).
- [31] I. Antoniadis and G. Leontaris, *Phys. Lett. B* **216**, 333 (1989).
- [32] R. Jeannerot, S. Khalil, G. Lazarides, and Q. Shafi, *J. High Energy Phys.* **10**, 012 (2000).
- [33] I. Antoniadis and G.K. Leontaris, *Phys. Lett. B* **216**, 333 (1989).
- [34] I. Antoniadis, G.K. Leontaris, and J. Rizos, *Phys. Lett. B* **245**, 161 (1990).
- [35] G. K. Leontaris and J. Rizos, *Phys. Lett. B* **510**, 295 (2001).
- [36] L. L. Everett, G. L. Kane, S. F. King, S. Rigolin, and L.-T. Wang, *Phys. Lett. B* **531**, 263 (2002).
- [37] P. Anastasopoulos, G. K. Leontaris, and N. D. Vlachos, *J. High Energy Phys.* **05**, 011 (2010).
- [38] A. H. Chamseddine, A. Connes, and W. D. van Suijlekom, *J. High Energy Phys.* **11**, 132 (2013).
- [39] G. Lazarides and C. Panagiotakopoulos, *Phys. Lett. B* **337**, 90 (1994).
- [40] B. Ananthanarayan, G. Lazarides, and Q. Shafi, *Phys. Rev. D* **44**, 1613 (1991).
- [41] M. Gómez, G. Lazarides, and C. Pallis, *Phys. Rev. D* **61**, 123512 (2000).
- [42] M. Carena, S. Pokorski, M. Olechowski, and C. E. M. Wagner, *Nucl. Phys. B* **426**, 269 (1994).
- [43] R. Hempfling, *Phys. Rev. D* **49**, 6168 (1994).
- [44] L. J. Hall, R. Rattazzi, and U. Sarid, *Phys. Rev. D* **50**, 7048 (1994).
- [45] A. Anandakrishnan, B. Bryant, and S. Raby, arXiv:1411.7035.
- [46] P. Skands et al., *J. High Energy Phys.* **07**, 036 (2004).
- [47] M. Gómez, G. Lazarides, and C. Pallis, *Nucl. Phys. B* **638**, 165 (2002).
- [48] G. Lazarides and C. Pallis, hep-ph/0406081.
- [49] N. Karagiannakis, G. Lazarides, and C. Pallis, *Int. J. Mod. Phys. A* **28**, 1330048 (2013).
- [50] N. Karagiannakis, G. Lazarides, and C. Pallis, *Phys. Rev. D* **87** (2013).
- [51] M. Gómez, G. Lazarides, and C. Pallis, *Phys. Rev. D* **67**, 097701 (2003).
- [52] N. Karagiannakis, G. Lazarides, and C. Pallis, *Phys. Lett. B* **704**, 43 (2011).
- [53] N. Karagiannakis, G. Lazarides, and C. Pallis, *PoS CORFU2011*, 023 (2011).
- [54] N. Karagiannakis, G. Lazarides, and C. Pallis, *J. Phys. Conf. Ser.* **384**, 012012 (2012).
- [55] B. C. Allanach, *Comput. Phys. Commun.* **143**, 305 (2002).
- [56] G. Belanger, F. Boudjema, P. Brun, A. Pukhov, S. Rosier-Lees, P. Salati, and A. Semenov, *Comput. Phys. Commun.* **182**, 842 (2011).
- [57] D. Pierce, J. Bagger, K. Matchev, and R.-J. Zhang, *Nucl. Phys. B* **491**, 3 (1997).
- [58] M. Carena, D. Garcia, U. Nierste, and C. E. M. Wagner, *Nucl. Phys. B* **577**, 88 (2000).
- [59] K.A. Olive et al. (Particle Data Group), *Chin. Phys. C*, **38**, 090001 (2014).
- [60] K. Tobe and J. Wells, *Nucl. Phys. B* **663**, 123 (2003).
- [61] ATLAS, CDF, CMS, and D0 Collaborations, arXiv:1403.4427.
- [62] LEPSUSYWG, ALEPH, DELPHI, L3, OPAL Experiments, URL <http://lepsusy.web.cern.ch/lepsusy>.
- [63] The ATLAS Collaboration, Tech. Rep. ATLAS-CONF-2013-061 (2013).
- [64] H. Abe, T. Kobayashi, and Y. Omura, *Phys. Rev. D* **76**, 015002 (2007).
- [65] D. Horton and G. Ross, *Nucl. Phys. B* **830**, 221 (2010).
- [66] J. Younkin and S. Martin, *Phys. Rev. D* **85**, 055028 (2012).
- [67] H. Abe, J. Kawamura, and H. Otsuka, *Prog. Theor. Exp. Phys.* **2013**, 013B02 (2013).
- [68] I. Gogoladze, F. Nasir, and Q. Shafi, *Int. J. Mod. Phys. A* **28**, 1350046 (2013).
- [69] T. Yanagida and N. Yokozaki, *Phys. Lett. B* **722**, 355 (2013).
- [70] T. Yanagida and N. Yokozaki, *J. High Energy Phys.* **11**, 020 (2013).
- [71] A. Delgado, M. Quiros, and C. Wagner, *J. High Energy Phys.* **04**, 093 (2014).
- [72] P. H. Chankowski and L. Slawianowska, *Phys. Rev. D* **63**, 054012 (2001).

- [73] F. Mahmoudi, *Comput. Phys. Commun.* **180**, 1579 (2009).
- [74] G. Belanger, F. Boudjema, A. Pukhov, and A. Semenov, *Comput. Phys. Commun.* **177**, 894 (2007).
- [75] M. Ciuchini, G. Degrassi, P. Gambino, and G. Giudice, *Nucl. Phys. B* **527**, 21 (1998).
- [76] F. Borzumati and C. Greub, *Phys. Rev. D* **58**, 074004 (1998).
- [77] G. Degrassi, P. Gambino, and G. Giudice, *J. High Energy Phys.* **12**, 009 (2000).
- [78] E. Barberio et al. (Heavy Flavor Averaging Group), arXiv:0808.1297.
- [79] M. Misiak et al., *Phys. Rev. Lett.* **114**, 221801 (2015).
- [80] M. Czakon et al., *J. High Energy Phys.* **04**, 168 (2015).
- [81] G. Isidori, F. Mescia, P. Paradisi, and D. Temes, *Phys. Rev. D* **75**, 115019 (2007).
- [82] M. Davier, A. Hoecker, B. Malaescu, and Z. Zhang, *Eur. Phys. J. C* **71**, 1515 (2011).
- [83] F. Jegerlehner and R. Szafron, *Eur. Phys. J. C* **71**, 1632 (2011).
- [84] K. Hagiwara, R. Liao, A. Martin, D. Nomura, and T. Teubner, *J. Phys. G* **38**, 085003 (2011).
- [85] T. Aoyama, M. Hayakawa, T. Kinoshita, and M. Nio, *Phys. Rev. Lett.* **109**, 111808 (2012).
- [86] G. Bennett et al. (Muon g-2 Collaboration), *Phys. Rev. D* **73**, 072003 (2006).
- [87] S. Martin and J. Wells, *Phys. Rev. D* **64**, 035003 (2001).
- [88] L. Covi, L. Roszkowski, R. de Austri, and M. Small, *J. High Energy Phys.* **06**, 003 (2004).
- [89] K.-Y. Choi, L. Covi, J. Kim, and L. Roszkowski, *J. High Energy Phys.* **04**, 106 (2012).
- [90] H. Baer and H. Summy, *Phys. Lett. B* **666**, 5 (2008).
- [91] H. A. Baer, M. Haider, S. Kraml, S. Sekmen, and H. Summy, *J. Cosmol. Astropart. Phys.* **02**, 002 (2009).
- [92] H. Baer, A. Box, and H. Summy, *J. High Energy Phys.* **10**, 023 (2010).
- [93] D. Akerib et al. (LUX Collaboration), *Phys. Rev. Lett.* **112**, 091303 (2014).
- [94] E. Aprile et al. (XENON100 Collaboration), *Phys. Rev. Lett.* **109**, 181301 (2012).
- [95] G. Belanger, F. Boudjema, A. Pukhov, and A. Semenov, *Comput. Phys. Commun.* **180**, 747 (2009).
- [96] M. Drees and M. Nojiri, *Phys. Rev. D* **48**, 3483 (1993).
- [97] G. Belanger, F. Boudjema, A. Pukhov, and A. Semenov, *Comput. Phys. Commun.* **185**, 960 (2014).
- [98] P. Shanahan, A. Thomas, and R. Young, *Phys. Rev. D* **87**, 074503 (2013).
- [99] *Brown University's Particle Astrophysics Group*, URL <http://dmtools.brown.edu>.
- [100] J. Lewin and P. Smith, *Astropart. Phys.* **6**, 87 (1996).
- [101] A. Green, *J. Cosmol. Astropart. Phys.* **08**, 022 (2007).
- [102] A. Green, *J. Cosmol. Astropart. Phys.* **07**, 005 (2008).
- [103] R. Catena and P. Ullio, *J. Cosmol. Astropart. Phys.* **08**, 004 (2010).
- [104] G. Bertone, D. Cerdeno, M. Fornasa, R. de Austri, and R. Trotta, *Phys. Rev. D* **82**, 055008 (2010).
- [105] V. E. Mayes, *Int. J. Mod. Phys. A* **28**, 1350061 (2013).
- [106] E. Aprile et al. (XENON1T Collaboration), *Springer Proc. Phys.* **148**, 93 (2013).
- [107] D. C. Malling et al., arXiv:1110.0103.
- [108] M. Aartsen et al. (IceCube Collaboration), *Phys. Rev. Lett.* **110**, 131302 (2013).